Bull Volcanol (2013) 75:732
DOI 10.1007/s00445-013-0732-3

RESEARCH ARTICLE

Origin and evolution of the Deception Island caldera (South Shetland Islands, Antarctica)

Joan Martí · Adelina Geyer · Gerardo Aguirre-Diaz

Received: 6 April 2013 / Accepted: 20 May 2013 / Published online: 5 June 2013

Abstract Deception Island has been interpreted variously as a classical ring fault caldera, as a tectonically controlled collapse caldera or as a tectonic depression. Review of previous studies combined with new fieldwork has allowed us to obtain a more precise model of the formation and internal structure of the Deception Island caldera. It formed as a result of the explosive eruption of basaltic-to-andesitic magmas, mostly as pyroclastic density currents representing in total a bulk volume of the order of 90 km^3. Caldera collapse occurred rapidly along a polygonal structural network consisting of several pre-existing major normal faults. These faults, which originated as a result of regional tectonics, controlled pre- and post-caldera volcanism on the island. The formation of the caldera generated a very active geothermal system inside its depression, which is responsible for most of the present-day seismic activity and may also have a significant influence on the observed surface deformation. Our results do not support the hypothesis that there is a large but shallow, active magma chamber beneath the current caldera; instead we suggest that recent eruptions have been fed by small batches of deeper-sourced magmas. The intrusive remains of these eruptions and probably of other minor intrusions that have not reached the surface provide the main heat source that sustains the current geothermal system.

Keywords Caldera · Tectonic depression · Faults · Volcanism · Current geothermal system

Editorial responsibility: S. Self

J. Martí (✉) · A. Geyer
Instituto de Ciencias de la Tierra Jaume Almera, CSIC,
LLuis Solé Sabaris s/n,
08028 Barcelona, Spain
e-mail: joan.marti@ictja.csic.es

G. Aguirre-Diaz
Centro de Geociencias, Campus UNAM-Juriquilla,
Santiago de Querétaro, Querétaro CP 76230, Mexico

Introduction

Deception Island is the most active volcano in the South Shetland Islands—Antarctic Peninsula group, and over 20 eruptions are known to have taken place there over the last two centuries (Pallàs et al. 2001; Smellie et al. 2002). It is located in the spreading centre of the Bransfield Strait marginal basin and consists of a < 0.75-Ma (Valencio et al. 1979; Smellie 1988) horseshoe-shaped stratovolcano, with a below-sea-level diameter of 25 km (Smellie 1988; Barclay et al. 2009) and an above-sea-level diameter of around 13 km (Fig. 1). A sea-flooded depression known as Port Foster, considered to be the caldera, occupies the central part of the island. Several periods of contrasting styles of volcanic activity can be distinguished (Smellie et al. 2002).

Two models have been proposed to explain the origin of the Deception Island caldera: (1) the caldera suffered a piston-like collapse following a major eruption around either a 'standard' (for the time) ring fault (Hawkes 1961; González-Ferrán and Katsui 1970; Baker et al. 1975; Walker 1984; Smellie 1988, 1989) or a series of regionally induced intersecting faults (Smellie 2001; Smellie et al. 2002) or (2) the caldera would correspond to a volcanic–tectonic depression formed progressively by passive (non-volcanic) extension along sets of faults linked to the regional extension that is unrelated to any specific caldera-forming eruptive event (Martí et al. 1996). The morphological features of Deception Island (the existence of a depression in the centre of the island, the apparent circular shape of the caldera rim, the location of post-caldera vents along the edge of the depression, etc.) support the former idea. However, its tectonic structure and the epicentral location of its seismicity on the main structural trends (Vila et al. 1992; Martí et al. 1996; Ibañez et al. 2003; Fernández-Ibañez et al. 2005; Maestro et al. 2007; Ben-Zvi et al. 2009; Zandomeneghi et al. 2009; Carmona et al. 2010) suggest that strong tectonic control in the formation of the caldera and the post-collapse evolution of the island has taken place (Martí et al. 1996; Smellie et al. 2002).

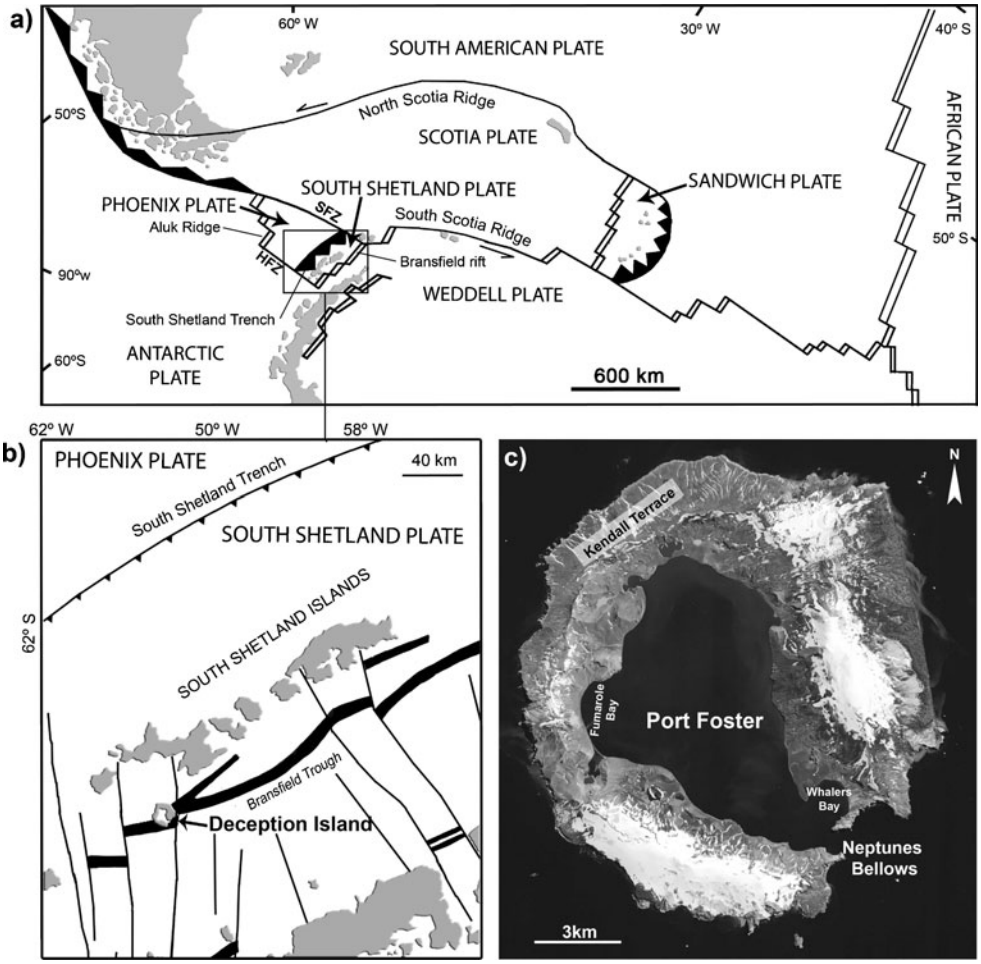

Fig. 1 **a** Simplified regional tectonic map and location of the South Shetland Islands (modified from Ibañez et al. (2003)). *HFZ* Hero Fracture Zone, *SFZ* Shetland Fracture Zone. **b** Location of Deception Island (modified from Grad et al. 1992). **c** Deception Island orthophotomap (http://lagc.uca.es/web_lagc/orto.jpg)

To date, a detailed event chronology and assessment of the caldera's origin and volcanic evolution is still lacking. However, based on new fieldwork conducted during the austral summer of 2010–2011 and a revision of the existing information gathered by previous geological and geophysical studies, we propose here an internally consistent model for the formation of the caldera. In this contribution, we (1) identify the part of the stratigraphic succession that is clearly related to the formation of the caldera, (2) determine the role that the pre-caldera tectonic structures played in the formation of the caldera, (3) analyse the dynamics of the caldera-forming eruption based on the sedimentological characteristics and petrology of syn-caldera deposits, and (4) discuss the influence of the caldera structure and its geothermal system on its current activity.

Geological setting

Deception Island is located at the south-west end of the Bransfield Strait, a young (< 1.4 Ma), < 60-km-wide, 500-km-long marginal basin that separates the South Shetland Islands from the Antarctic Peninsula (Fig. 1). This strait is a back-arc basin of the South Shetland Islands volcanic arc (Fig. 1), which was formed as a consequence of the Phoenix plate subduction under the Antarctic plate during the upper Mesozoic–Cenozoic interval (Dalziel 1984). This convergence ceased 3.3 Ma ago when the Phoenix plate stopped spreading (Fig. 1) (Lawver et al. 1996; Livermore et al. 2000). The opening of the Bransfield rift generated a new microplate, the South Shetland Plate (Fig. 1), bounded by the Shackleton and Hero Fracture Zones to the east and west, respectively, by the South Shetland Trench to the north and by the Bransfield rift to the south. The Bransfield basin has a characteristic graben structure, with tilted blocks and rotational faults developed in a regime of continental extension (Jefffers and Anderson 1990; Gracia et al. 1997; Vaun et al. 2005). The edge of the Bransfield basin is defined by a spreading centre with which Deception, Penguin and Bridgeman islands and a number of submerged volcanic vents are associated. Deception Island is located near the intersection between the tensional axis of the Bransfield basin and the extension of the Hero Fracture Zone (Fig. 1).

Deception Island corresponds to a composite volcanic complex, the construction of which was truncated by the formation of the central caldera (Fig. 2). All exposed rocks

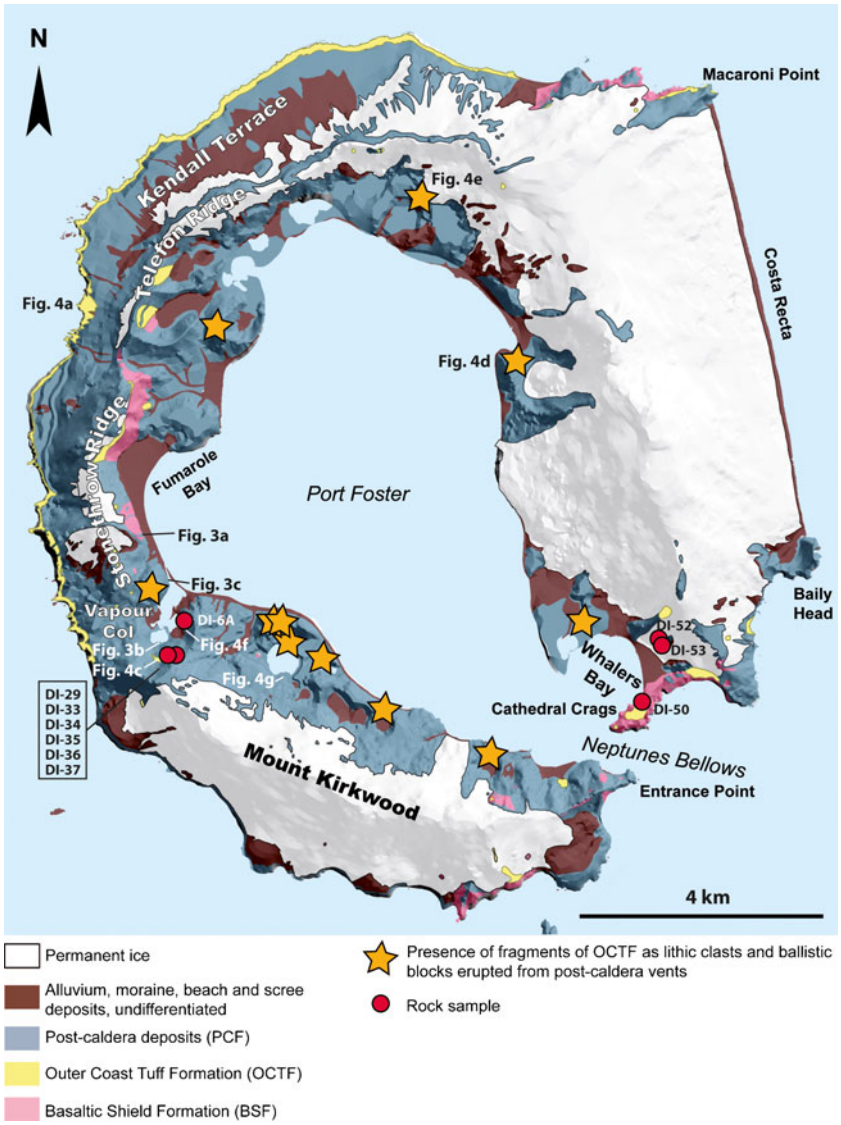

Fig. 2 Simplified geological map of Deception Island (modified from Martí and Baraldo (1990) and Smellie et al. (2002)) and location of the analysed rock samples

have normal magnetic polarity, indicating that they are less than 0.75 Ma (Valencio et al. 1979). On the basis of K–Ar data, Keller et al. (1991) indicate that most of the subaerial part of the island was built in the last 0.2 Ma, while Smellie (2001), based on a correlation between the Deception Island deposits and the tephra found elsewhere in the region, suggests that all the exposed rocks appear to be late Pleistocene–Recent (probably < 100 ka). The lack of geochronological data from the Deception Island rocks and the fact that none of the tephra studies conducted in the Antarctic region (see Pallas et al. (2001); Smellie 1999) has been able to identify deposits related to the formation of the caldera prevent establishing a precise age for this event. However, assuming that most of Deception Island corresponds to the pre-caldera shield structure and that only post-caldera tephra of middle Holocene age to present has been recognised in the tephrochronological studies of the Antarctic region (see Smellie (1999) and references herein), we speculate that the formation of the caldera could have occurred in late Pleistocene–early Holocene.

Methodology

This study included new fieldwork, the aim of which was to (1) identify and characterise the stratigraphy of the caldera-forming units, (2) revise the tectonic structure of Deception Island and (3) collect samples for petrological study. Fieldwork was conducted during the austral summer of 2010–2011; all information collected was digitalised and entered into a database using an open-source GIS framework (QGIS, www.qgis.org) with, as a cartographic base, a panchromatic orthophoto with a spatial resolution of 0.6 m per pixel and projection UTM, datum WGS84, zone 20 South.

We analysed the whole rock and mineral chemistry of all the samples collected, which included the full stratigraphic

succession of Deception Island; nevertheless, only the results corresponding to the samples from the caldera-forming units are given in this study. The whole rock analyses were performed by the GeoAnalytical Laboratory at Washington State University using X-ray fluorescence (XRF) and inductively coupled plasma mass spectrometry facilities. With XRF, the relative error of the measurements is under 1 % for both major and trace elements, under 5 % for the REE and under 10 % for the remaining trace elements. Chips of juvenile samples were mounted in epoxy resin, polished and then analysed for major elements of mineral phases and groundmass with a CAMECA SX-50 electron microprobe at Barcelona University. The combination of silicates and oxides was used for calibration. A 20-μm-diameter defocused beam was used for groundmass analyses in order to minimise Na migration.

Stratigraphy

Previous stratigraphic studies of Deception Island essentially only considered whether the rock units pre- or post-date the formation of the caldera (see Hawkes 1961; González-Ferrán and Katsui 1970; Baker et al. 1975; Smellie 1988, 1989, 2001; Martí and Baraldo 1990; Birkenmajer 1992; Baraldo and Rinaldi 2000). By means of a comparison of previously published stratigraphic successions, Smellie (2001) offered a detailed revision of the stratigraphy of Deception Island and formally defined its stratigraphic units. In this study, however, we use a simplified version of Smellie's stratigraphy—a comprehensive description of the lithostratigraphy of Deception Island is found in the original work (Smellie 2001).

The oldest pre-caldera succession is clearly unrelated to the formation of the caldera and corresponds to most of a now-submerged volcanic shield, in which different eruptive cycles and vents can be distinguished (Smellie 2001). Several successions of volcanic rocks, mainly of mafic composition with unconformable contacts between them, were constructed. Although Smellie (2001) distinguished different discordant units in the pre-caldera sequence, we propose here a simplification and thus group all of these units in the shield building phase or basaltic shield formation (BSF) given that their eruption dynamics, products and stratigraphy do not differ (Fig. 3). Most of these units correspond to lava flows and different types of Strombolian deposits and hyaloclastitic breccias, mainly palagonitised and indurated by alteration processes. The basal boundary is not exposed but probably corresponds to an unconformable contact with Cretaceous–Tertiary consolidated sedimentary and volcanic rocks and/or unconsolidated and poorly consolidated pre-Quaternary marine sediments deposited on the submerged South Shetland Islands platform (Ashcroft 1972; Grad et al. 1992; Smellie 2001).

A thick succession of palagonitized pyroclastic density current (PDC) deposits of mafic-to-intermediate composition, known as the Outer Coast Tuff Formation (OCTF) (Hawkes 1961; Smellie 2001), overlays unconformably these shield-related units and forms an almost continuous outcrop along the outer part of the island extending from Macaroni Point to Vapour Col and inland around and inside Port Foster (Figs. 2 and 3). The OCTF is formed by several units of massive yellow tuff, each 1–15 m in thickness, which are characterised by a lack of internal stratification, flat bases and existence locally of incipient columnar jointing (Smellie 1988,1989; Martí and Baraldo 1990) (Fig. 4a). These deposits are poorly sorted and contain abundant lithic clasts (up to 35 %) of basalt and basaltic-andesite derived from the BSF, together with vesiculated, porphyric juvenile pyroclasts of similar compositions, ranging in size from fine lapilli to bombs (Fig. 4b). Juvenile vesiculated fragments are sometimes flattened. Lithic blocks up to 50 cm in diameter are common throughout the OCTF and are conspicuous as thick lenses repeated at several levels in which the content of lithic clasts is as high as 80 %; the rest of this deposit has a matrix similar to that of the other OCTF deposits (Fig. 4c).

The populations of lithic clasts in the OCTF deposits differ between sectors of the island. These lithic-rich units contain abundant gabbroic xenoliths. The matrix of the OCTF pyroclastic deposits comprises small lithic clasts originating from the BSF rocks, crystal fragments and devitrified glass shards. The morphology of the glass shards and juvenile scoria fragments is angular, sometimes block-like. A number of finely laminated layers, occasionally with well-stratified, poorly sorted, lapilli- to ash-grained deposits, appear interbedded and in stratigraphic continuity with the massive deposits. These interbedded deposits are also very lithic rich and occasionally have cross-stratification. No major discontinuities that might suggest the existence of a break in the deposition in the order of 10–100 years or more are present in this pyroclastic sequence. Due to their characteristics, the massive PDC deposits can be classified as ignimbrites, while the grain size distributions and sedimentary structures of the interbedded laminated deposits suggest that all are derived from dilute pyroclastic surges. The lithic-rich units are interpreted as co-ignimbrite lithic breccias associated with the emplacement of the pyroclastic flows.

The OCTF PDC deposits are well exposed on the northern and western coasts, where they form a 16-km long continuous cliff in which individual deposits exhibit a remarkable continuity and nearly constant thickness (only a very gentle dip of up to 5° toward the exterior of the island) (Fig. 2). Discontinuous outcrops of OCTF rocks exist in other sectors of the outer part of the island, as well as inland around Port Foster at Stonethrow Ridge, Telefon Ridge, Vapour Col, Mount Kirkwood, Cathedral Crags and

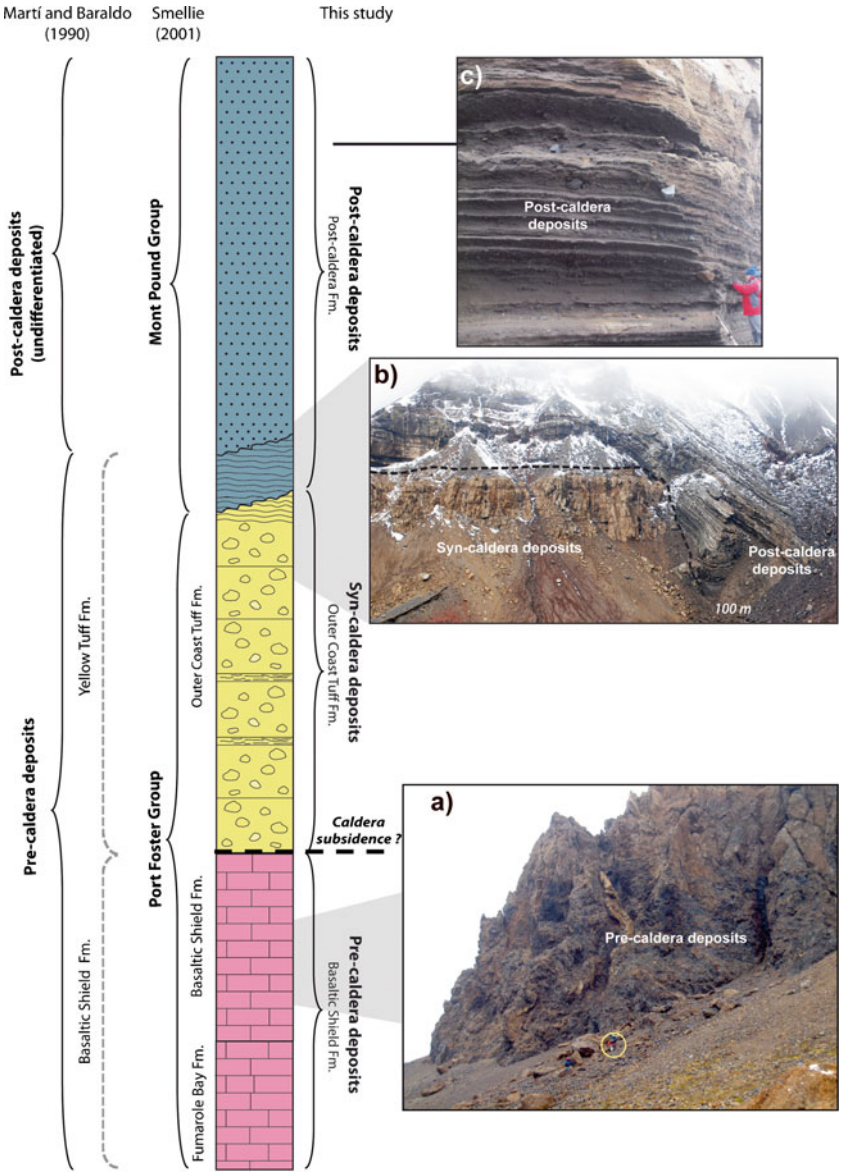

Fig. 3 Synthetic stratigraphic section of Deception Island indicating at the sides of the stratigraphic log the divisions proposed in previous studies (on the *left*) and the present work (on the *right*). **a** Detail of the Basaltic Shield Formation at Fumarole Bay (see Fig. 2 for location). **b** Image of the Vapour Col succession illustrating the uncomfortable contact between the syn-caldera and post-caldera deposits (see Fig. 2 for location). **c** Example of post-caldera deposits at Vapour Col (see Fig. 2 for location)

Whalers Bay (Fig. 2). On the outer coast, the OCTF has an average thickness of 45–60 m, reaching a maximum of 90 m at some points, while around Vapour Col, where the base and top of the OCTF are well exposed, it has a total thickness of 92 m.

The OCTF succession is cut by the borders of the caldera and is overlaid unconformably by discontinuous sequences of post-caldera deposits related to different vents, most of them located inside or around the caldera depression (Fig. 3). The post-caldera volcanism can be subdivided into different members of stratigraphic relationships not discussed in this work (see Smellie (2001) for more detail).

The presence of abundant fragments of OCTF as lithic clasts and ballistic blocks emitted by some of the many post-caldera vents that border Port Foster is remarkable (Figs. 2 and 4d, e) and indicates that the OCTF is also present in the collapsed sector of Deception Island. The existence of intra-caldera OCTF rocks is also confirmed by several seismic reflection profiles and tomographic studies that were obtained from inside Port Foster (see below), which provide information on the stratigraphy and tectonics of the infill sequence (Grad et al. 1992; Rey et al. 1995; Martí et al. 1996; Ben-Zvi et al. 2009; Zandomeneghi et al. 2009. Luzón et al. 2011).

Petrology and geochemistry

Most of the OCTF juvenile fragments correspond in size to lapilli and are highly vesicular, glassy fragments with a crystal content of 3–14 %, and have phenocryst assemblages of various proportion and composition. Although most of these juvenile components range in size from several centimetres to just a few millimetres, a few bomb-size clasts with angular

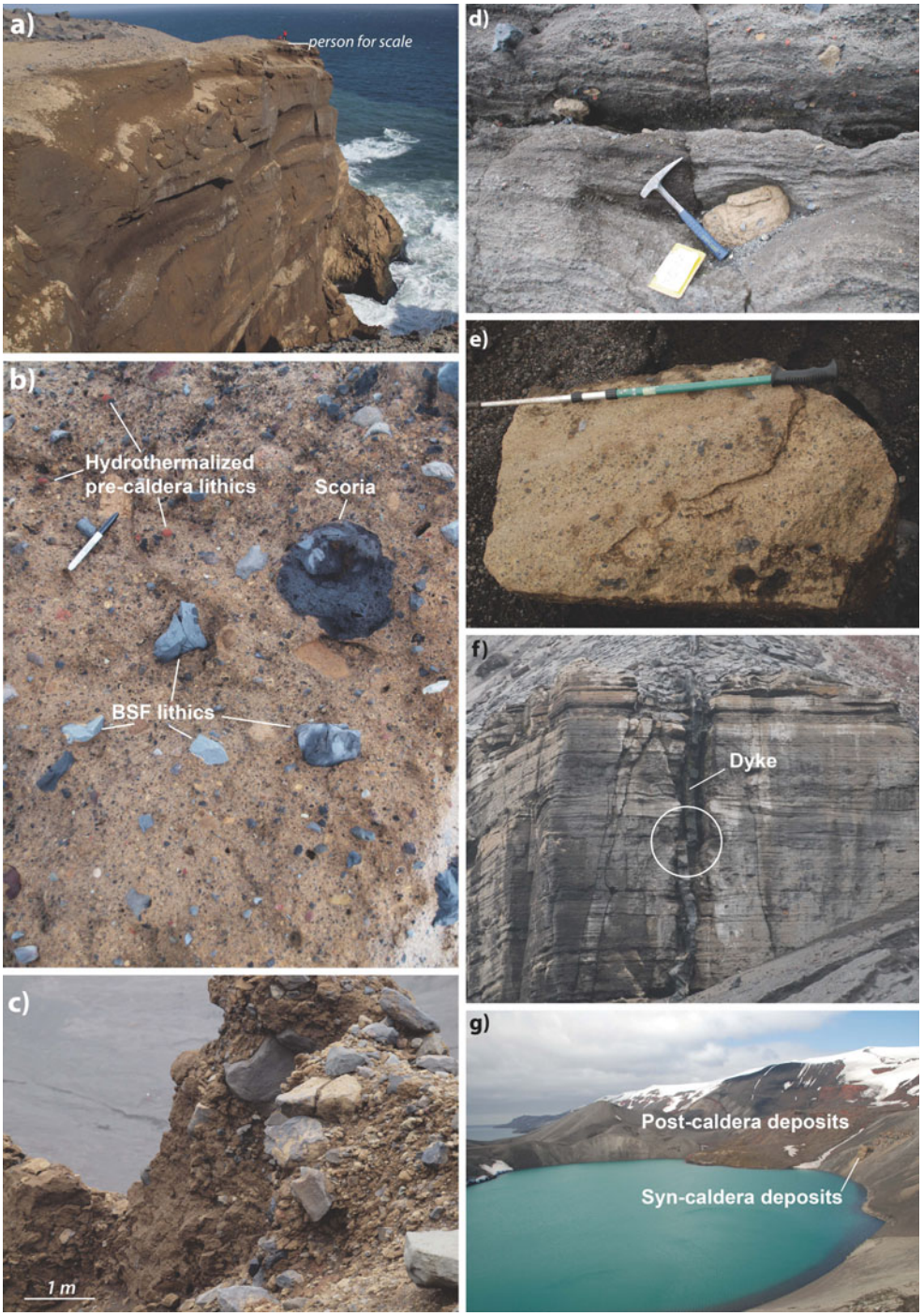

Fig. 4 **a** Image of the Outer Coast Tuff Formation from one of the cliffs along Kendall Terrace (see Fig. 2 for exact location). **b** Detail of the Outer Coast Tuff Formation showing the abundance of lithics from the Basaltic Shield Formation (*BSF lithics*). **c** Lithic-rich breccia interbedded in the Outer Coast Tuff Formation interpreted as co-ignimbrite lithic breccias associated with the emplacement of the pyroclastic flows (see Fig. 2 for exact location). **d**, **e** Fragments of the Outer Coast Tuff Formation as lithic clasts and ballistic blocks erupted from numerous post-caldera vents around Port Foster (see Fig. 2 for exact location). **f** Dyke showing evidence of post-intrusive tectonic extension (*white circle*) (see Fig. 2 for exact location). **g** Image of Crater Lake where it is possible to observe along the walls some outcrops of Outer Coast Tuff Formation covered by the post-caldera deposits

shapes have also been found. Occasionally, these juvenile components have fluidal textures and stretched gas bubbles (vesicles). The juvenile lapilli fragments contain small-sized (< 2 mm) phenocrysts of intermediate plagioclase, augite and hypersthene pyroxenes, fayalite olivine, magnetite and ilmenite (Table 1). Plagioclase phenocrysts are euhedral to subeuhedral, exhibit multiple twining and are occasionally zoned (normal and reverse zonings). Olivine phenocrysts are always rounded and on some occasions have embayments, thus suggesting a certain disequilibrium with the liquid. Pyroxene phenocrysts are euhedral to sub-euhedral and commonly have internal fractures. Magnetite and ilmenite phenocrysts are always euhedral. The groundmass that surrounds the phenocrysts is formed of small crystal fragments and completely devitrified pseudomorphs of vitroclasts. Application of the clinopyroxene-glass geobarometre (Putirka 2008) gives a pressure in the order of 150–200 MPa, equivalent to a depth of 4–6 km.

Table 1 Microprobe analysis of mineral phases and glasses of juvenile fragments from the Outer Coast Tuff Formation

	Olivines										Pyroxenes								Fe–Ti oxides
	DI29aA	DI29aC	DI29aF	DI33A	DI33A2	DI33A3	DI33B2	DI33B3	DI52		DI29aC	DI29aD	DI29aD2	DI29aH	DI30L2	DI30L3	DI35F	DI35F	DI35H
Si Ox%	38.36	38.58	38.25	38.57	38.22	38.32	39.33	38.79	38.41		50.45	49.4	52.17	50.33	49.87	51.12	51.12	51.22	0.81
Ti Ox%	0	0	0.01	0.02	0.01	0.02	0.02	0.04	0.03		1.11	1.43	0.51	1.04	1.25	0.95	0.9	0.8	16.94
Al Ox%	0	0.03	0.01	0.01	0.02	0.02	0.01	0.02	0		3.11	3.83	1.64	2.99	3.73	2.66	3.4	3.35	1.23
Fe Ox%	18.16	17.89	18.21	14.77	14.81	14.78	14.53	14.5	19.14		7.5	8.35	8.68	7.28	7.41	7.44	5.56	5.4	71.42
Mn Ox%	0.33	0.27	0.4	0.21	0.23	0.23	0.13	0.23	0.34		0.25	0.23	0.43	0.16	0.22	0.12	0.19	0.09	0.78
Mg Ox%	43.17	42.62	42.7	46.08	45.95	45.91	45.71	45.89	41.79		15.32	14.77	16.97	16.05	15.21	15.85	16.05	15.99	2.98
Ca Ox%	0.22	0.22	0.23	0.23	0.27	0.24	0.24	0.24	0.24		21.29	21.1	18.77	21.12	21.86	21.74	22.23	22.21	0.31
Na Ox%	0	0.03	0	0.01	0	0.01	0.01	0	0		0.42	0.45	0.34	0.32	0.33	0.32	0.26	0.3	4.35
K Ox%	0	0.01	0.01	0	0	0.01	0	0.01	0		0.03	0	0.01	0	0	0	0	0	0.02
Cr Ox%	0.05	0.07	0.03	0.03	0.04	0.05	0.04	0.06	0.01		0.17	0.06	0.04	0.14	0.09	0.07	0.34	0.39	0.39
Ni Ox%	0.17	0.15	0.09	0.14	0.11	0.12	0.2	0.09	0.07		0.03	0.06	0	0.1	0.04	0.01	0.06	0	0.04
Sum	100.45	99.87	99.94	100.06	99.65	99.72	100.23	99.87	100.04		99.68	99.66	99.57	99.52	100	100.27	100.12	99.76	99.27
Fo	80.91	80.94	80.69	84.76	84.69	84.7	84.87	84.94	79.56	En	43.98	42.66	48.03	45.45	43.36	44.46	45.66	45.71	
Fa	19.09	19.06	19.31	15.24	15.31	15.3	15.13	15.06	20.44	Fs	12.08	13.53	13.78	11.57	11.85	11.71	8.87	8.66	
										Wo	43.94	43.81	38.19	42.99	44.79	43.83	45.46	45.63	

	Glasses									Plagioclasses									
	DI30A1	DI30P3	DI-35-D	DI6aA1	DI6aL2	DI6aP1	DI29aQ1	DI29B2	DI37F3		DI29aB	DI29aC	DI30D	DI30D2	DI30D3	DI35B	DI35B1	DI6a5	DI6aG4	DI37I3
Si Ox%	56.83	54.69	55.48	52.58	53.37	49.14	49.54	55.1	48.89		52.68	51.98	53.09	52.04	51.87	46.73	46.45	48.64	51.3	47.88
Ti Ox%	2.31	2.56	1.87	2.23	2.14	2.79	1.63	1.54	1.93		0.11	0.1	0.06	0.07	0.08	0.05	0.05	0.22	0.06	0.02
Al Ox%	14.14	13.4	12.5	14.74	15.97	11.69	3.19	16.28	15.78		28.58	28.76	28.39	29.59	29.71	32.65	32.88	30.04	29.79	32.09
Fe Ox%	9.79	10.77	9.29	10.54	9.22	11.11	8.56	7.85	9.52		0.71	0.7	0.64	0.67	0.54	0.63	0.58	1.56	1.09	0.54
Mn Ox%	0.21	0.25	0.2	0.21	0.21	0.22	0.26	0.2	0.17											
Mg Ox%	2.67	3.96	5.75	3.82	3.42	5.88	15.29	3.94	7.24		0.08	0.17	0.11	0.12	0.19	0.12	0.05	0.27	0.06	0.11
Ca Ox%	5.53	7	9.94	7.48	8.4	12.86	19.82	7.48	10.03		11.8	12.57	12.06	13.18	13.41	16.32	16.79	13.91	13.13	15.86
Na Ox%	5.6	4.38	3.86	5.3	5.06	4.66	0.53	5	4.07		5.07	4.61	4.85	4.19	3.94	2.4	2.44	4.68	4.41	2.63
K Ox%	1.1	0.76	0.9	0.72	0.64	0.58	0.01	0.72	0.55		0.09	0.09	0.1	0.04	0.05	0.01	0.03	0.1	0.12	0.04
Cr Ox%	0.02	0	0.07	0.03	0.02	0	0.21	0.02	0.03											
Ni Ox%	0.01	0.06	0	0.06	0	0.03	0.02	0.07	0											
Sum	98.23	97.85	99.87	97.72	98.45	98.95	99.07	98.21	98.2		99.13	98.98	99.28	99.89	99.79	98.91	99.27	99.43	99.97	99.15
Fo										Ab	43.54	39.67	41.87	36.45	34.59	20.98	20.78	37.66	37.54	23.04
Fa										An	55.94	59.81	57.57	63.34	65.1	78.94	79.03	61.83	61.77	76.75
										Or	0.52	0.53	0.56	0.21	0.31	0.08	0.19	0.51	0.69	0.21

All the OCTF deposits underwent a palagonitic alteration that endowed them with their characteristic yellowish colour. This alteration has been interpreted as largely derived from the reaction with a pore-fluid, largely corresponding to water vapour that was incorporated into the system whenever the erupting magma interacted with an external water source (Martí and Baraldo 1990). This alteration particularly affected the vitric fragments but left the phenocrysts unaltered. The main alteration products are smectites, Fe oxides, zeolites (chabacite, analcime, phillipsite and faujacite) and calcite, which replace the vitric components and fill the gas vesicles (Martí and Baraldo 1990).

The OCTF pyroclastic deposits are characterised by a relatively high content (up to 35 %) in lapilli-sized lithic fragments that mostly consist of BSF-derived fragments. These are easily separable from the OCTF juvenile clasts by their rounded shape, microlitic texture and mineralogy. Moreover, a number of gabbroic xenoliths have also been found in these pyroclastic deposits, above all in the co-ignimbrite lag breccias. These xenoliths range from olivine gabbros containing olivine, plagioclase and minor clinopyroxene and amphibole to pyroxene gabbros with plagioclase, clinopyroxene and magnetite and have been interpreted as co-magmatic with the OCTF juvenile magma (Risso and Aparicio 2002). Other xenoliths of felsic composition have also been found and are thought to be accessory lithic fragments, probably derived from the underlying granitic basement (Risso and Aparicio 2002).

The results of the whole rock analysis of the OCTF rocks are given in Table 2. Although the original compositions may have been partially altered due to the palagonitization of the original glass (which would have caused a decrease in silica and CaO and an increase in alkalis), major element geochemistry of the OCTF juvenile components reveals a consistent differentiation trend from basalts to andesites, also compatible with the mineralogical assemblages found in these rocks (Fig. 5; Tables 1 and 2). This suggests the presence of a compositionally zoned magma chamber, whose existence is confirmed by some of the trace elements and the REE, which, having remained practically intact, provide good indications of the original composition of these rocks. However, this zonation trend does not have a stratigraphic correspondence as these different compositions coexist throughout the entire succession of the deposits. In addition to the thermal disequilibrium observed in the mineralogy of some juvenile fragments (e.g. normal and reverse zoning in some plagioclase phenocrysts and embayments in olivine phenocrysts), these fragments also contain textures—resulting from the mingling of magmas—in the form of flow banding with bands of different composition (basaltic and andesitic).

Tectonic structure

In previous works that used field geology, remote sensing and geophysical studies, several regional and local tectonic trends have been identified on Deception Island (Smellie 1988, 1989; Rey et al. 1995; Martí et al. 1996; González-Casado et al. 1999; Fernández-Ibañez et al. 2005; Maestro et al. 2007; Barclay et al. 2009; Zandomeneghi et al. 2009; Carmona et al. 2010). Although some of these trends are clearly visible in the field, others can only be inferred or correspond to more local effects such as gravitational loading during the construction of the post-caldera cones. This has caused some confusion and it remains unclear whether all these trends are realistic or whether they have any relationship with the tectonic evolution of the island; as a result, certain unexplained discrepancies between different studies exist. In order to minimise this problem, part of our fieldwork was designed to identify those structures that are recognisable in the field (Fig. 8). In addition, we incorporated into our structural revision the tectonic features that have been clearly identified in the seismic profiles conducted inside the caldera depression and around Deception Island (Rey et al. 1995; Martí et al. 1996; Barclay et al. 2009).

A NE–SW-oriented regional tectonic trend, almost parallel to the expansion axis of the Bransfield Strait, is clearly predominant on the island (Fig. 6); NW–SW- and N–S-oriented faults are also present. Several of the post-caldera tuff cones formed around the caldera border are highly fractured and faulted and show structural trends that are not always compatible with the main trends (González-Casado et al. 1999; Maestro et al. 2007; Paredes et al. 2006, 2007) corresponding to gravitational faults originated by the rapid growth (loading) of these phreatomagmatic edifices.

Bathymetric and shallow seismic reflexion studies carried out inside the caldera depression and around the island (Rey et al. 1995; Martí et al. 1996; Barclay et al. 2009) reveal that the infill sequence was affected by a well-developed NE–SW-oriented linear fracture system that has developed half-graben structures; this corresponds to the fracture system identified inland and offshore. Also of note is the presence of some tectonic and volcanic alignments inside Port Foster and around the island that are not parallel to the main alignments and appear to have a radial component (Barclay et al. 2009).

In addition, the few dykes that have been identified on Deception Island are always of mafic composition and intrude along NE–SW- and NW–SE-trending linear regional faults affecting both the pre- and post-caldera sequences. Occasionally, dykes are composite and have brittle deformations that suggest post-intrusive tectonic extensions (Fig. 4f).

Table 2 Chemical analyses of the syn-caldera (Outer Coast Tuff Formation) juvenile fragments collected for this study (see Fig. 2 for the exact location of the different samples)

	DI-6A	DI-29	DI-31	DI-33	DI-34	DI-35	DI-36	DI-37	DI-50	DI-52	DI-53
SiO_2	52.24	52.7	55.64	49.96	49.55	54.07	54.49	48.56	50	51.41	49.43
TiO_2	1.742	1.914	1.448	1.622	1.617	1.284	1.347	1.71	1.814	1.613	1.743
Al_2O_3	16.45	16.14	16.17	18.92	18.64	17.92	17.21	17.32	15.93	17.12	15.38
FeO*	8.78	9.19	7.42	8.42	8.21	7.12	7.35	8.33	9.17	8.37	8.79
MnO	0.161	0.175	0.157	0.148	0.147	0.141	0.147	0.149	0.17	0.156	0.163
MgO	4.94	4.21	3.89	6.38	6.33	4.6	4.35	5.67	5.25	5.59	5.02
CaO	9.11	8.36	6.91	10.7	10.56	9.13	8.45	9.67	9.89	9.97	10
Na_2O	4.18	4.55	5.14	3.73	3.69	4.28	4.57	3.85	3.87	4.04	4.06
K_2O	0.5	0.58	0.87	0.44	0.48	0.6	0.67	0.45	0.34	0.47	0.32
P_2O_5	0.268	0.29	0.254	0.275	0.266	0.214	0.228	0.276	0.26	0.241	0.252
Total	98.38	98.13	97.89	100.6	99.5	99.37	98.8	95.99	96.7	98.97	95.14
LOI (%)	0.33	0.86	1.67	0.13	0.12	−0.06	−0.12	2.68	2.91	−0.11	5.66
Ni	23	14	14	43	44	33	28	27	25	30	24
Cr	60	16	22	125	125	86	59	104	65	103	63
Sc	30	30	25	28	29	26	26	30	34	32	34
V	248	251	178	215	215	179	182	226	278	233	262
Ba	94	95	113	70	64	92	103	63	63	75	65
Rb	6	6	13	4	5	7	9	4	3	5	3
Sr	385	361	344	453	446	406	389	413	415	433	410
Zr	165	203	257	153	153	190	208	167	175	147	169
Y	30	38	39	26	25	31	33	31	33	29	32
Nb	6.5	6.9	8.9	8.1	8.2	6.2	6.8	8.4	5.2	5	4.9
Ga	17	21	20	17	18	20	19	18	18	20	17
Cu	52	43	52	41	40	68	86	37	67	62	66
Zn	75	85	82	66	65	68	74	65	80	73	76
Pb	4	3	4	3	1	4	4	2	3	4	3
La	12	11	15	9	9	11	11	7	11	9	11
Ce	24	29	36	21	23	30	28	27	24	24	27
Th	2	2	2	2	1	3	2	0	1	2	1
Nd	17	20	22	15	16	17	19	17	19	18	17
U	1	0	0	0	2	2	0	0	0	1	1
La	10.26	11.32	13.88	9.46	9.63	10.62	11.74	10.27	9.05	9.38	8.72
Ce	25.44	28.77	34.75	23.5	23.72	26.39	29.27	25.41	24.05	23.57	23.08
Pr	3.67	4.21	4.89	3.33	3.41	3.79	4.15	3.67	3.59	3.41	3.45
Nd	16.64	19.49	21.7	15.21	15.37	17.24	18.56	16.63	17.09	15.87	16.3
Sm	4.73	5.57	5.9	4.14	4.26	4.69	5.07	4.55	4.97	4.41	4.64
Eu	1.71	1.93	1.86	1.53	1.55	1.58	1.72	1.64	1.76	1.61	1.67
Gd	5.35	6.34	6.45	4.54	4.62	5.22	5.59	5.1	5.63	5.03	5.35
Tb	0.94	1.12	1.15	0.8	0.8	0.93	0.99	0.9	1	0.88	0.94
Dy	5.81	7.06	7.18	4.92	4.96	5.87	6.24	5.47	6.26	5.54	5.89
Ho	1.19	1.46	1.49	1.03	1.03	1.2	1.32	1.12	1.28	1.12	1.2
Er	3.22	3.91	4.16	2.74	2.72	3.31	3.55	3.04	3.45	3.03	3.31
Tm	0.46	0.57	0.62	0.39	0.38	0.48	0.53	0.43	0.49	0.43	0.47
Yb	2.81	3.5	3.81	2.35	2.39	3.01	3.28	2.65	3.05	2.64	2.93
Lu	0.46	0.55	0.59	0.38	0.37	0.47	0.53	0.42	0.47	0.41	0.46
Ba	88	89	112	58	59	91	99	60	62	71	60
Th	1.12	1.28	1.92	0.75	0.77	1.44	1.6	0.88	0.78	1.29	0.77
Nb	5.34	5.62	7.09	6.75	6.9	5.13	5.66	6.88	4.16	4.14	4.04

Table 2 (continued)

	DI-6A	DI-29	DI-31	DI-33	DI-34	DI-35	DI-36	DI-37	DI-50	DI-52	DI-53
Y	30.46	36.69	38.06	25.26	25.45	30.44	33.14	28.01	32.09	28.13	30.48
Hf	3.82	4.71	5.91	3.27	3.33	4.32	4.77	3.64	3.96	3.46	3.77
Ta	0.43	0.42	0.52	0.49	0.5	0.38	0.43	0.52	0.32	0.3	0.31
U	0.33	0.36	0.57	0.26	0.27	0.41	0.46	0.28	0.24	0.32	0.23
Pb	3.26	3.6	4.83	1.91	2.01	3.65	4.2	2.24	2.45	3.73	2.44
Rb	6.1	5.9	12.7	3.1	3.7	7.4	8.4	3.5	2.1	4.8	2.5
Cs	0.39	0.31	0.59	0.13	0.15	0.38	0.45	0.23	0.08	0.23	0.17
Sr	391	360	343	449	442	400	390	412	419	433	408
Sc	31.9	29.4	24.7	28.9	29.3	26.2	26.3	28.9	35.1	33.1	32.9
Zr	164	199	253	148	149	185	207	162	172	147	163

Oxides in Wt. %; trace elements and REE in ppm

LOI loss on ignition

Geophysical studies

In addition to the bathymetric and shallow seismic reflection data mentioned earlier, other geophysical studies have provided relevant data for the purpose of this study. The available bathymetric data show that the floor of Port Foster is morphologically regular, as indicated by the continuity of the bathymetric lines (Rey et al. 1992). It is characterised by the presence of a littoral platform with an average width of 700 m. A break of slope on the platform occurs at a depth of 50–60 m and is followed by a steep incline down to a depth of 120 m. Beyond this point, the floor of the bay is uniform and dips gently inward to reach a maximum depth of 195 m in its centre. A few submerged volcanic edifices or sedimentary structures disturb locally the uniformity of the floor of the depression. The bathymetry of the floor shows no topographical evidence for localised resurgence as proposed by Cooper et al. (1998) but does reveal a broad uplift of the eastern side of the caldera, which could have been caused either by high sediment supply rates from the east of the island or by a trap-door caldera deformation with its minimum subsidence in the east (Barclay et al. 2009).

Luzón et al. (2011) describe the shallow velocity structure at nine different sites around Port Foster using correlations of ambient seismic noise (Fig. 7a). They concluded that the structure beneath these sites consists in the first 400 m of two layers with thicknesses of about 100 and 300 m and S-wave velocities around 0.2–0.8 and 0.7–1.1 km/s, respectively, which they interpret as being post-caldera deposits composed of relatively soft pyroclastic layers and sediments with different degrees of compaction. Given that all the sites studied by Luzon et al. (2011) are located at the margin of the caldera depression, these deposits should correspond to either debris avalanche deposits formed by the gravitational collapse of the caldera wall, post-caldera volcanic deposits or scree and alluvial fan deposits. A further increase in the S-wave velocity indicates the position of the transition between these soft sediment

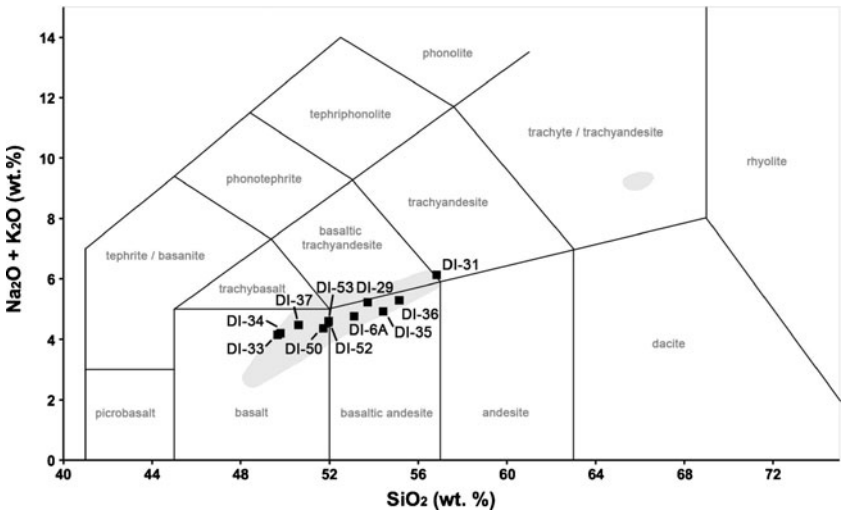

Fig. 5 TAS diagram showing the range in compositions normalized to 100 % of syn-caldera juvenile fragments collected for this study. Light- and dark- shaded regions correspond to the compositional range of the Outer Coast Tuff and pre-caldera (Basaltic Shield Formation and Fumarole Bay Formation) samples analysed by Smellie et al. (2002)

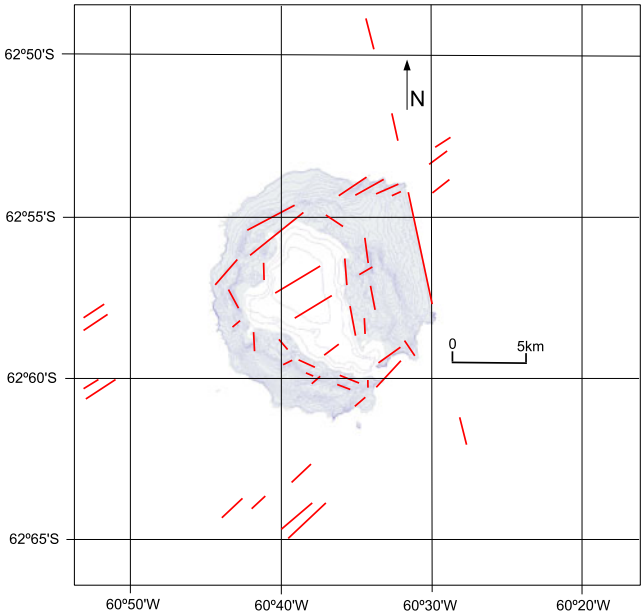

Fig. 6 Simplified structural map of Deception Island and surrounding areas indicating the main tectonic lineation identified in the field (this work) and also in bathymetric (Barclay et al. 2009) and seismic (Rey et al. 1995; Martí et al. 1996) studies (see text for more explanation)

layers and the harder 1–1.2-km-thick layers that lie above the rock units with S-wave velocities up to 4.5 km/s.

Previous studies have revealed that the seismo-stratigraphic succession at Port Foster also consists of three main geophysical units characterised by similar S-wave velocities. The lower unit corresponds to a velocity region of 4.5 km/s that represents the basement of the Port Foster depression (Grad et al. 1992; Ben-Zvi et al. 2009). The middle unit is a 1.2-km-thick layer of 2.5–3.5 km/s assumed to correspond to consolidated pyroclastic material (Ashcroft 1972; Grad et al. 1992; Ben-Zvi et al. 2009). The upper unit is formed of a <100-m-thick succession of low velocity post-caldera sediments and recent volcanic deposits produced during the final eruptions (Rey et al. 1995, 2002; Ben-Zvi et al. 2009). The Port Foster infill sequence is occasionally discontinuous, highly fractured and intruded by several dykes (Grad et al. 1992; Rey et al. 1995).

Recent seismic tomography studies on Deception Island (Ben-Zvi et al. 2009; Zandomeneghi et al. 2009) have found a pronounced low-velocity anomaly beneath Port Foster that extends to a depth of 5.5 km and reaches its maximum velocity perturbation at a depth of 1–2 km. The presence of this low-velocity zone represents a combination of, on the

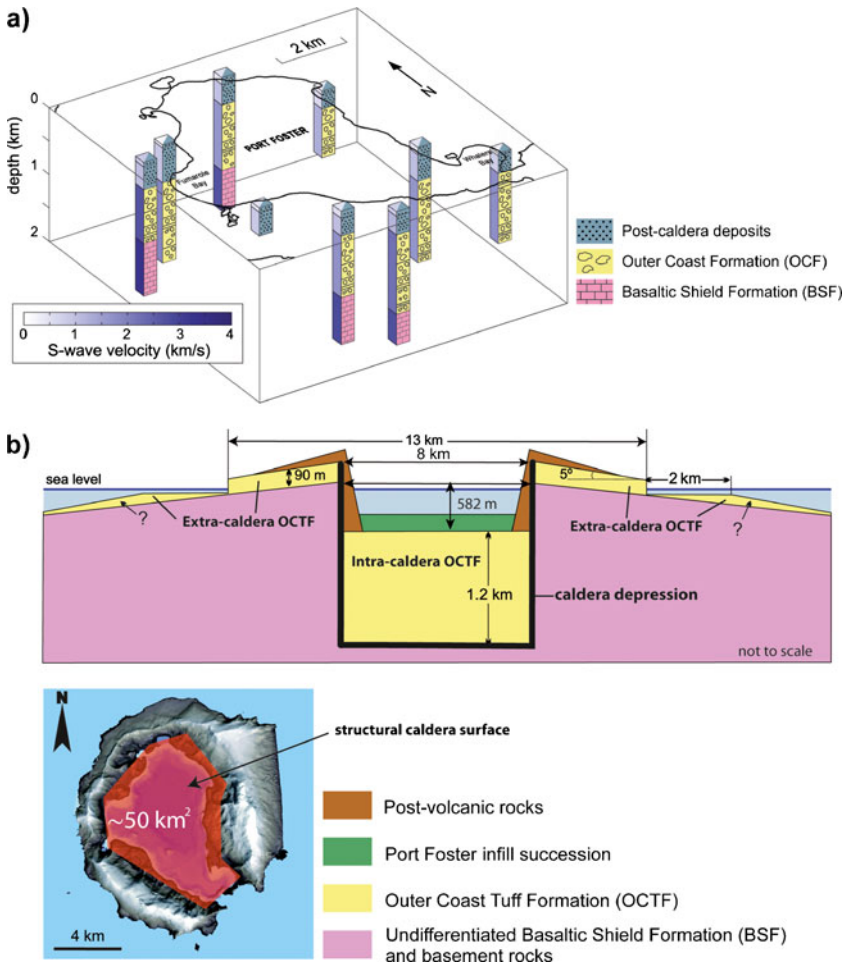

Fig. 7 **a** Sketch of the S-wave velocity structures derived at sites along the inner coastline of Deception Island. Only the well-constrained layers combined with a volcano-stratigraphic interpretation of the deposits are shown (modified from Luzón et al. (2011)). **b** Sketch illustrating the main parameters used to estimate the caldera depression volume, as well as the extra- and intra-caldera volume of the Outer Coast Tuff Formation

one hand, low-velocity post-caldera sediments infilling Port Foster overlaying a 1.2–1.4-km-thick layer of 3.5 km/s underlain by a higher-velocity region of 4.5 km/s (Grad et al. 1992; Ben-Zvi et al. 2009) and, on the other, the existence of high temperatures and partial melt (Ben-Zvi et al. 2009). As a result of this interpretation of the seismic data (Ben-Zvi et al. 2009; Zandomeneghi et al. 2009), the occurrence of a 1.2–1.4-km-thick sedimentary layer above a large magma chamber extending downwards from 2 km to at least 5 km in depth has been proposed. These authors indicate that, despite the low velocities (which may also be due to the presence of high temperatures or of altered or fractured rocks), the magnitude of the anomaly is consistent with the presence of a significant volume of partial melt. Similar conclusions are reached by Pedrera et al. (2013) on the basis of a magnetotelluric survey and topographic parametric sonar data.

Discussion

Stratigraphy

On the basis of stratigraphic relationships and volume calculations, Smellie (2001) and Smellie et al. (2002) suggested that there is a genetic relationship between the OCTF and the formation of the Deception Island caldera. This contradicts the model described by Martí et al. (1996), who proposed that, due to passive collapse imposed by regional tectonics, the caldera formed a long time after the deposition of the OCTF. Our field revision detailed earlier confirms that the OCTF rocks, which are cut by the caldera border, constitute the only stratigraphic unit that can account for a caldera-forming eruption. This conclusion is reinforced if we accept that the seismic stratigraphy inside the caldera depression is composed of an uppermost layer of unconsolidated post-caldera deposits, a thick intermediate layer corresponding to the OCTF rocks and a basement formed by the BSF rocks (Fig. 7a). According to this description, the presence of the OCTF rocks both outside and inside the caldera depression, the significant variation in thickness found at each site and the fact that they are unconformably overlaid by the first post-caldera deposits all suggest that the OCTF was deposited synchronously with the main phase in the formation of the caldera, as suggested by Smellie (2001). The caldera collapse may have occurred somewhat after the deposition of the OCTF and/or the original caldera border may have been enlarged by erosion since some of the earlier post-caldera deposits have also been cut by the caldera. We found no evidence of collapse breccias that could have formed as a result of the instability of the recently formed caldera border (see Lipman 1976); nevertheless, they could be buried by post-caldera volcanism, particularly near the caldera border where the succession of post-caldera deposits is much thicker as has been revealed by previous geophysical studies (see Luzón et al. 2011). Therefore, in the context of a volcanic–stratigraphic analysis, we conclude that the thick pyroclastic succession of OCTF should definitively be interpreted as the caldera-forming unit, as was suggested by Smellie (2001) and Smellie et al. (2002).

Volume of deposits and caldera volume

The total volume of the caldera depression and, consequently, the size of the eruption correspond to the sum of the volume of the caldera-forming deposits emplaced inside and outside the caldera depression. The volume of the caldera depression can be estimated by multiplying the size of the structural caldera surface by the maximum vertical displacement of the topmost pre-caldera units affected by the caldera collapse. Part of this volume is occupied by caldera-forming deposits emplaced in the depression while it was forming and by post-caldera sediments emplaced afterwards. The remaining part of the caldera is empty and is now occupied by seawater. The volume of this empty part of the caldera plus the volume corresponding to post-caldera deposits should correspond to the volume of syn-caldera deposits emplaced outside the caldera.

The exact distribution and variation in the thickness of the extra-caldera OCTF rocks deposited inland is not known since they have been partly eroded and/or covered by post-caldera products. As well, most of the OCTF deposits were emplaced offshore or inside the caldera depression, and so their exact thickness and distribution can only be inferred by indirect geophysical methods (see Grad et al. 1992; Rey et al. 1995; Ben-Zvi et al. 2009; Luzón et al. 2011). However, a first-order estimate of the volume of the caldera depression and that of the OCTF can be obtained if a few simple assumptions are made.

The present morphological border of the caldera encloses a surface area of approximately 82 km^2 but cannot be used to estimate the volume of the caldera given that there is clear evidence that it has been enlarged by erosion. Instead we have to use the structural limits of the caldera, which theoretically correspond to the original limits of the caldera depression. The structural limits of the Deception Island caldera are not visible but, as part of a first-order approach, can be inferred by joining together the post-caldera vents surrounding the caldera depression that contain erupted blocks of OCTF rocks (Fig. 2). The resulting structural border, with an irregular polygonal shape in which most of the sides correspond to the main fractures or structural trends that have been verified in this study (Fig. 6), encloses an area of approximately 50 km^2 (Fig. 7b), 65 % smaller than the current morphological size of the caldera. The highest point of the caldera border at which we have found

BSF rocks lies SW of Entrance Point (Fig. 2) at an altitude of 322 m a.s.l. The present floor of Port Foster Bay in the centre of the depression is located at a depth of 180 m b.s.l. but becomes progressively shallower toward its edges. Previously presented geophysical data (Grad et al. 1992; Ben-Zvi et al. 2009) suggest that the thickness of the intra-caldera deposits overlaying the pre-caldera basement in the centre of the depression is about 1.28 km. Therefore, the total vertical displacement suffered by the Deception Island caldera was 1.78 km (322+180+1,280 m), and the total volume of the resulting depression was 89 km^3.

The bulk volume of extra-caldera OCTF deposits should be equivalent or a little bit larger than the total volume of the caldera minus the bulk volume of the intra-caldera OCTF deposits. If the thickness of the intra-caldera OCTF deposits is about 1.2 km, the volume of the intra-caldera OCTF deposits will be in the order of 60 km^3, which gives a remaining volume for the depression of nearly 29 km^3. To calculate the volume of the extra-caldera OCTF, first, we have to estimate the volume of the outcropping deposits. Although the OCTF deposits are only exposed as a continuous outcrop along the north-western part of the outer coast, they also appear as smaller and discontinuous outcrops, overlaying unconformably the BSF, at other points of the outer coast (e.g. Macaroni Point) and inland (e.g. Cathedral Crag) (Fig. 2). Even though in some cases the OCTF in these outcrops is only a few metres thick (probably due to extensive erosion), this distribution still indicates that the OCTF was emplaced radially over nearly the whole of the island. If we also take into account the continuity of the main OCTF outcrop (about 16 km), as well as its nearly constant thickness and flat dip, characteristics that are also observed in other outcrops (e.g. Vapour Col), it is logical to assume that the OCTF covered Deception Island with a mantle of more or less of constant thickness. Assuming an average thickness of 90 m (corresponding to the thickness measured in the outcrops where the OCTF is well exposed such as on the outer coast and at Vapour Col) and a mean diameter of 13 km for the whole island and of 8 km for the caldera depression, the part of the OCTF emplaced on the currently emerged part of Deception Island can be estimated to have a total volume of 7.4 km^3.

The outside of Deception Island has been deeply eroded by the sea, and so an important part of the original OCTF volume has been removed. Due to a lack of precise seismic and bathymetric information, we were not able to perform an accurate estimate of the extent of the offshore OCTF deposits and their average thickness. However, we can calculate the original subaerial part that has been removed by marine erosion from the dimensions and geometries given in Fig. 7b (assuming that the island has suffered no significant isostatic movements after the caldera formation). This gives a total volume of about 2 km^3. In addition, we should estimate the volume of the material expelled into the atmosphere and transported far from the vent by the ash clouds that accompanied the emplacement of the pyroclastic gravity currents; this corresponds to about 15 % of the total erupted volume if we compare the crystal content of the juvenile fragments with that of the matrix, following Walker (1972). Assuming that the total volume of erupted material was equivalent to the original volume of the caldera depression, this means that the volume of missing material will be in the order of 13 km^3 (89 $km^3 \times 0.15$)

If we sum all the calculated partial bulk volumes, we obtain a minimum volume for the extra-caldera OCTF of about 23 km^3, which is a little less than the volume of the caldera depression that was not infilled with intra-caldera OCTF deposits. If we could add to the calculated volume of extra-caldera deposits the submarine part of these deposits, we believe that the total volume of the extra-caldera deposits would match that of the non-infilled part of the caldera depression.

If we assume an average lithic content of 30 % in the OCTF deposits, we reach a figure of about 26 km^3 for the total bulk volume of the caldera-forming products corresponding to the host rock that was excavated during the eruption and incorporated into the OCTF deposits as lithic fragments; the rest would account for the volume of magma erupted during the caldera event. This means that the eruptible magma had a volume of at least 63 km^3 (89 km^3 - 26 km^3)—or a little less—if we transform these values into DRE. Compared to other collapse calderas (see Geyer and Martí (2008) and http://www.gvb-csic.es/CCDB.htm), the Deception Island caldera should thus be classified as a medium-sized caldera of similar dimensions to that of Krakatau and Santorini.

The Deception Island caldera-forming eruption was large enough to have produced a layer of pyroclastic material that should be recognisable in marine sediments and in ice records from the area. Nevertheless, previous studies of tephra deposits have failed to identify any such material (Pallàs et al. 2001; Fretzdorff and Smellie 2002). The identification of this marker would provide crucial information for dating this important eruption and for correlating the different stratigraphic sequences whilst improving knowledge of the time-scale of the volcanic and geodynamic pulses in the Bransfield Strait.

Eruption dynamics

Our results suggest that although the erupted magma came from a compositionally zoned magma chamber, this zonation was not preserved during magma withdrawal, thereby suggesting that different parts of the magma chamber were simultaneously withdrawn. Smellie et al. (1992, 2002) suggest that the eruption of the OCTF involved the interaction

of two magma series and that the influx of fresh magma into a stratified magma chamber might have been responsible for destabilising the chamber and for triggering the OCTF eruption. Despite its limitations, our geochemical and mineralogical data appear to confirm this hypothesis. However, we are unable to confirm whether the basaltic magma identified in our study is the basic member of the differentiation system or whether it represents a fresh input of magma intruded into a compositionally stratified andesitic magma chamber. The presence of normal and reverse zoning in some plagioclase phenocrysts and of embayments in the olivine phenocrysts suggests the existence of thermal disequilibrium in the magma chamber prior to the eruption, which might indicate the intrusion of fresh magma. However, there is no evidence of chemical mixing, and so the time elapsed between the intrusion and the eruption must have been relatively short and probably only allowed for physical mingling. Evidence for mingling between the magmas in the pyroclasts indicates a disequilibrium interaction that may have occurred during the eruption, as is shown in magma recharge and withdrawal models of caldera-forming eruptions (Folch and Martí 1998; Folch et al. 2001).

The lack of internal stratigraphic discontinuities indicates that most of the OCTF sequence formed in a very short period of time, probably during a single eruptive event. The distribution of the deposits over the whole island, the continuity of some of these units and their relatively constant thickness all suggest that the OCTF was emplaced radially from the caldera borders, mantling older deposits (BSF) and progressively infilling the caldera depression.

The OCTF is entirely composed of deposits originating from pyroclastic density currents and no associated fallout deposits have been identified. Massive, lithic-rich, thick ignimbrites are predominant and contain a number of interbedded pyroclastic surge units in stratigraphic continuity. This suggests that the eruptions responsible for their generation immediately developed into massive proportions, thereby causing the continuous collapse of the mixtures of gas and pyroclasts before they developed into stable eruption columns. This process was favoured by the incorporation of a large amount of lithic fragments into the eruptive mixture, which, in addition to increasing its density, also lowered its temperature (see Martí et al. (1991)) and thus reduced its ability to incorporate and expand atmospheric air at the vent that would have helped establish buoyant columns. The consistent and large amount of lithics found in these pyroclastic deposits suggests as well a continuous opening/erosion of the eruption conduits, which would also have contributed to the instability of the eruption. Although most of the lithic clasts are rounded, the juvenile scoria fragments are angular, which suggests that, on the one hand, no abrasion of the lithic clasts occurred during the emplacement of the PDCs but that, on the other, there was strong friction between these clasts in the conduit. The co-ignimbritic lag breccia deposits that appear interbedded and on top of the main OCTF sections (outer coastline and Vapour Col) are rich in co-magmatic lithics, which suggests that there was significant erosion of the deeper part of the feeding systems, which probably also affected the magma chamber.

The hydrovolcanic nature of some of the OCTF deposits—the product of a magma/water interaction—still remains to be explained. Smellie (2001) and Smellie et al. (2002) identified a number of changes in sea level during the evolution of Deception Island that suggest that while the upper part of the BSF was entirely subaerial, the earliest volcanic episodes in the island's geological record were submarine. These authors proposed that at the time of the caldera-forming eruption, the sea level was higher and so most of the OCTF were below sea level, which would explain why water was able to flood the erupting conduits. However, the lack of hydrovolcanic fragmentation in some of the deposits suggests that the magma/water interaction was not continuous during the whole caldera-forming eruption, which would contradict the theory of a submarine environment for the eruption. Alternatively, occasional magma/water interaction could have been favoured by a number of factors: the existence of marine intrusion into the basaltic shield, the entrance of sea water into the eruption conduits through the faults that controlled the caldera collapse, the melting of an ice cap or even the opening of the collapsing caldera into the sea due to a failure of the volcanic edifice in its southern sector (Entrance Point). In addition, the lack of stratigraphic evidence such as marine terraces would seem to rule out a submarine caldera-forming eruption, and so we suggest that the caldera eruption mostly occurred in a subaerial environment.

Structural controls on caldera collapse

Contrary to the conclusions of a number of previous studies (e.g. Hawkes 1961; González-Ferrán and Katsui 1970; Baker et al. 1975; Walker 1984; Smellie 1988, 1989), Deception Island is neither a classical ring fault caldera nor a tectonic depression formed by the passive foundering of intracaldera blocks (Martí et al. 1996). As already inferred by Smellie (2001) and Smellie et al. (2002), the island in fact corresponds to a volcanic–tectonic caldera formed during the massive emptying of a shallow magma chamber, in which the caldera subsidence was completely controlled by pre-existing faults.

Most of the Deception Island faults and fracture systems are compatible with the NW–SE oblique extension of the Bransfield Strait and affect both pre- and post-caldera rocks, thereby indicating that they have controlled the location of volcanic activity since the beginning of the construction of Deception Island up to the present day. Although more local

tectonic effects caused by the inflation of a shallow magma chamber and subsequent caldera formation could also have occurred (Smellie 2001; Smellie et al. 2002; Pérez-López et al. 2007), there is no doubt that the faults that controlled the caldera collapse are related to the main regional trends. Examples of collapsed calderas of different sizes in which tectonic control plays an important part are not uncommon (Martí 1991; Branney and Kokelaar 1994; Aguirre-Díaz et al. 2008; Acocella 2010). The same structural framework that controlled the formation of the Deception Island caldera is still controlling tectonic seismicity and deformation at present as can be deduced from recent geophysical studies (Berrocoso et al. 2008; Carmona et al. 2010).

The existence of a well-defined pre-caldera orthogonal fault system that affected the entire island, as well as the characteristics of the OTCF succession, accounts for a rapid, strongly fault-controlled caldera collapse episode (Fig. 8), in which different caldera blocks subsided more or less synchronously into the magma chamber. The fact that some of these faults are visibly affecting pre- and post-caldera sediments in the seismic profiles carried out inside Port Foster (Rey et al. 1995) also supports this idea. Moreover, the concentration of lithic fragments of different composition and provenance in units of the OCTF located at opposite sites on the island also give credence to the idea of the opening of different vent fractures. However, the rapid deposition of post-caldera materials into the Port Foster depression buried the topographically irregular caldera floor under a homogenous carpet that has been shown to be relatively flat by bathymetric surveys.

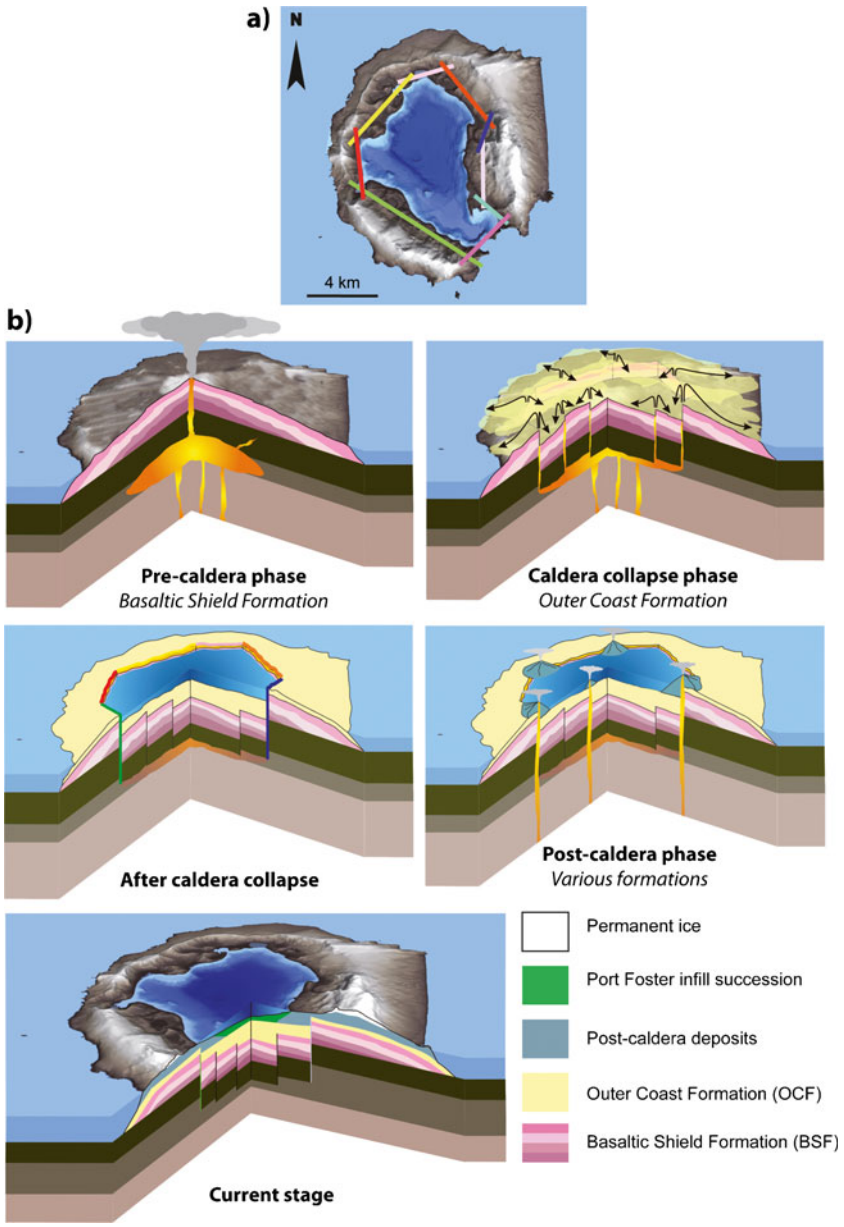

Fig. 8 **a** Sketch illustrating the network of tectonic faults that acted as normal faults during the formation of the caldera depression. **b** Simplified sketch illustrating the formation of the Deception Island caldera

The fact that the Deception Island caldera is bounded by pre-existing tectonic faults rather than by a ring fault suggests that both the emplacement and extent of the magma chamber were also controlled by these faults. Although the timing of caldera collapse with respect to the eruption of the OCTF is unclear, the presence of considerably thicker OCTF deposits in the form of caldera infill suggests that it started earlier in the eruption. This agrees with the fact that in tectonic calderas, caldera collapse tends to occur earlier in the process given that the conduits through which the magma will escape from the chamber have already been formed (Martí et al. 2009). The whole OCTF sequence is cut by the caldera border and is overlain unconformably by localised tuff cone deposits that formed after caldera subsidence. Some of these deposits (e.g. Vapour Col) are also cut by the present caldera border, thereby indicating that either caldera subsidence continued for some time after the caldera eruption or the caldera border has retreated due to subsequent erosion.

Current subvolcanic system

The seismic tomography model presented by Ben-Zvi et al. (2009) and Zandomeneghi et al. (2009) invokes the presence of a 150-km^3 magma reservoir at a very shallow depth (2–5 km). This is also supported by Pedrera et al. (2013) on the basis of a magnetotelluric study. However, the results of our study and other previous studies of caldera formation are inconsistent with such a model. First, caldera collapse episodes tend to empty all the eruptible magma from the associated magma chamber (Martí et al. 2000). As a result, the magma chamber is either partially or totally destroyed. This causes a significant change in the stress field, which in turn will lead to a change in the mechanical conditions for magma accumulation at the same depth. In fact, when a collapse caldera forms, it is mechanically difficult to return to the same stress conditions as before in order to create a new magma chamber of the same extent and volume as the previous one (Geyer and Martí 2009). In the case of Deception Island, the formation of the collapse caldera caused the structural perturbation of its central zone to a depth of 4–5 km, giving rise to a highly fractured pre-caldera basement, now covered by a thick pile of syn- and post-caldera deposits. The depth reached by the caldera fracturing can be estimated by considering the depth (4–6 km according to the petrological data) at which magma accumulated before the caldera eruption, which would correspond to the depth given in this study. After the caldera was formed, this highly fractured zone was almost certainly intruded by deeper magmas that fed the post-caldera volcanism and caused a thermal perturbation of the rocks below Port Foster. In addition, this whole zone developed a geothermal system that hydrothermally altered all the rocks above and significantly reduced their strength. This is probably the main reason for the low seismic velocities and high conductivities observed. Furthermore, the volume of magma—around 150 km^3—that, according to tomographic studies (Ben-Zvi et al. 2009; Zandomeneghi et al. 2009), would have accumulated in this low-velocity zone is nearly three times the volume of magma that caused the caldera eruption and so is clearly unrealistic. The geothermal system of Deception Island is very active and shows clear signs of activity including fumaroles, seismic tremors and other long-period signals, as well as inflation and deflation episodes, which indicate a high permeability of the medium and little chance of retaining such a large amount of over-pressurised magma for long periods of time. Finally, the eruptions that have occurred on Deception Island during the post-caldera period have all small volumes (0.01–0.1 km^3) of magma which, given the improbability of having been fed by a large magma chamber, are more likely to be linked to small batches of magma that fed each eruption individually.

Conclusions

Deception Island is a complex volcanic system formed on the spreading axis of the Bransfield Strait (Antarctica). Its whole evolution has been controlled by the action of regional tectonic lineaments formed in response to the back-arc geodynamics of this strait. Volumetrically, the main episode in the formation of the island corresponds to the construction of a basaltic shield complex that constitutes the main part of the island, most of which is submerged. Multiple vents and volcanic episodes, mostly generating lava flows and Strombolian pyroclastic and hyaloclastitic deposits, can be recognised in the emerged parts of this basaltic shield. The construction of this shield edifice was truncated by the formation of a collapse caldera in the centre of the island. This caldera was originated by the eruption of a shallow, compositionally zoned magma chamber, which was probably triggered by a magma-mixing episode. The caldera-forming products correspond to the Outer Coast Tuff Formation, mainly composed of a thick sequence of massive ignimbrites and minor pyroclastic surge deposits of basaltic to andesitic composition. The caldera collapse episode occurred rapidly during or after a single eruptive event and was entirely controlled by the numerous tectonic faults that already existed and that facilitated the downward movement of the caldera blocks. The formation of the caldera caused the destruction of the associated magma chamber, thus permitting the deeper magmas that feed the post-caldera volcanism to re-ascend, mainly using as pathways the same fractures and faults that controlled the caldera collapse. This situation has continued until the present day and still controls the frequency and type of recent volcanism. After the formation of the central caldera, a large hydrothermal system developed in the interior of the depression using the

highly fractured pre-caldera basement and syn-caldera rocks. This hydrothermal system is currently very active and is responsible for most of the observed volcanic–tectonic seismicity and surface deformation.

Acknowledgments This research was supported by MICINN grants CTM2009-05919-E and CGL2010-22022-C02-02. AG had a Juan de la Cierva Grant (JCI-2010-06092). We warmly thank José Manuel Lupiani and all the military staff of the Antarctic Base Gabriel de Castilla for their logistic support and constant help, without which this research would have been impossible. We would also like to thank the Associate Editor Steve Self and John Smellie and Joachim Gottsmann for their detailed and constructive reviews.

References

Acocella V (2010) Coupling volcanism and tectonics along divergent plate boundaries: collapsed rifts from central Afar. Ethiopia Geol Soc Am Bull 122:1717–1728. doi:10.1130/B30105.1

Aguirre-Díaz GJ, Labarthe-Hernández G, Tristán-González M, Nieto-Obregón J, Gutiérrez-Palomares I (2008) The ignimbrite flare-up and graben caldera of the Sierra Madre Occidental, Mexico. In: Gottsmann J, Martí J (eds) Caldera volcanism: analysis, modeling and response. Elsevier, Amsterdam, pp 143–174

Ashcroft WA (1972) Crustal structure of the South Shetland Islands and Bransfield Strait, 1st edn. British Antarctic Survey, London, 43 p., 1 fold. leaf p

Baker P E, McReath I, Harvey, MR, Roobol MJ, Davies, TG (1975) The geology of the South Shetland Islands: volcanic evolution of Deception Island. British Antarctic Survey Scientific Reports 78: 81 pp

Baraldo A, Rinaldi CA (2000) Stratigraphy and structure of Deception Island, South Shetland Islands, Antarctica. Jour South Am Earth Sci 13:785–796

Barclay AH, Wilcock WSD, Ibañez JM (2009) Bathymetric constraints on the tectonic and volcanic evolution of Deception Island Volcano, South Shetland Islands. Antarctic Sci 21:153–167. doi:10.1017/S0954102008001673

Ben-Zvi T, Wilcock WSD, Barclay A, Zandomeneghi D, Ibáñez JM, Almendros J (2009) The P wave velocity structure of Deception Island, Antarctica, from two-dimensional seismic tomography. Jour Volcanol Geotherm Res 180:67–80

Berrocoso M et al (2008) Geodetic research on Deception Island and its environment (South Shetland Islands, Bransfield Sea and Antarctic Peninsula) during Spanish Antarctic campaigns 1987–2007. In: Capra A, Dietrich R (eds) Geodetic and geophysical observations in Antarctica. Springer, Berlin, pp 97–123. doi:10.1007/978-3-540-74882-3_6

Birkenmajer K (1992) Volcanic succession at Deception Island, West Antarctica: a revised lithoestratigraphic standard. Studia Geologica Polonica 101:27–82

Branney MJ, Kokelaar BP (1994) Volcanotectonic faulting, soft-state deformation, and rheomorphism of tuffs during development of a piecemeal caldera, English Lake District. Geol Soc Am Bull 106:507–530

Carmona E, Almendros J, Peña JA, Ibáñez JM (2010) Characterization of fracture systems using precise array locations of earthquake multiplets: an example at Deception Island volcano, Antarctica. J Geophys R 115, B06309. doi:10.1029/2009JB006865

Cooper APR, Smellie JL, Maylin J (1998) Evidence for shallowing and uplift from bathymetric records of Deception Island. Antarctica Antarctic Sci 10:455–461

Dalziel, I.W.D. (1984) Tectonic evolution of a ForearcTerrane. Southern Scotia Ridge, Antarctica. Geol. Soc. Am. Pec. Pap. 200, 32 pp.

Fernández-Ibañez F, Perez-Lopez R, Martinez-Diaz JJ, Paredes C, Giner-Robles JL, Caselli AT, Ibañez JM (2005) Costa Recta beach, Deception Island, West Antarctica: a retreated scarp of a submarine fault? Antarctic Sci 17:418–426

Folch A, Martí J (1998) Generation of overpressure in felsic magma chambers by replenishment. Earth Planet Sci Lett 163:301–314

Folch A, Codina R, Martí J (2001) Numerical modelling of magma withdrawal during caldera-forming eruptions. J Geophys Res 106:16163–16175

Fretzdorff S, Smellie JL (2002) Electron microprobe characterization of ash layers in sediments from the central Bransfield basin (Antarctic Peninsula): evidence for at least two volcanic sources. Antarct Sci 14(4):412–421

Geyer A, Martí J (2008) The new worldwide collapse caldera database (CCDB): a tool for studying and understanding caldera processes. J Volcanol Geotherm Res 175:334–354

Geyer A, Martí J (2009) Stress fields controlling the formation of nested and overlapping calderas: implications for the understanding of caldera unrest. J Volcanol Geotherm Res 181:185–195

González-Casado JM, López-Martínez J, Giner J, Duran JJ, Gumiel P (1999) Analsis de la microfracuración en la Isla Decepción. Antártida Occidental Geogaceta 26:27–30

González-Ferrán O, Katsui Y (1970) Estudio integral del volcanismo cenozoico superior de las Islas Shetland del Sur, Ant/mica. Instituto Antártico Chileno Serie Científica 1:123–174

Gracia E, Canals M, Farran ML, Prieto MJ, Sorribas J (1997) Morphostructure and evolution of the Central and Eastern Bransfield Basins (NW Antarctic Peninsula). Marine Geophys Res 18:429–448

Grad M, Guterch A, Sroda P (1992) Upper crustal structure of Deception Island area, Bransfield Strait, West Antarctica. Antarctic Sci 4:469–476

Hawkes, D.D. (1961) The geology of the South Shetland Islands: II. The geology and petrology of Deception Island. Falkland Islands Dependencies Survey Scientific Reports, 27, 43 pp.

Ibañez J, Almendros J, Carmona E, Martínez-Arévalo C, Abril M (2003) The recent seismo-volcanic activity at Deception Island volcano. Deep-Sea Res II 50(2003):1611–1629

Jefffers JD, Anderson JNB (1990) Sequence stratigraphy of the Bransfield Basin, Antarctica: implications for tectonic history and hydrocarbonpotentia1. In: St. John B (ed) Antarctica as an exploration frontier: hydrocarbon potential, geology and hazards. Am Ass Petrol Geol Stud Geol 31:13–29

Keller RA, Fisk MR, White WM, Birkenmajer K (1991) Isotopic and trace element constraints on mixing and melting models of marginal basin volcanism, Bransfield Strait, Antarctica. Earth Planet Sci Lett 111:287–303

Lawver LA, Sloan BJ, Barker DHN, Ghidella M, Von Herzen RP, Keller RA, Klinkhammer GP, Chin CS (1996) Distributed, active extension in Bransfield Basin, Antarctic Peninsula: evidence from multibeam bathymetry. GSA Today 6:1–6

Lipman PW (1976) Caldera-collapse breccias in the western San Juan Mountains, Colorado. Geol Soc Am Bull 87:1397–1410

Livermore R, Balanyá JC, Maldonado A, Martínez JM, Rodríguez-Fernández J, Sanz de Galdeano C, Galindo Zaldívar J, Jabaloy A, Barnolas A, Somoza L, Hernández-Molina J, Suriñach E, Viseras C (2000) Autopsy on a dead spreading center: the Phoenix Ridge, Drake Passage. Antarctica Geol 28:607–610

Luzón F, Almendros J, García-Jerez A (2011) Shallow structure of Deception Island, Antarctica, from correlations of ambient seismic noise on a set of dense seismic arrays. Geophys J Int 185:737–748

Maestro A, Somoza L, Rey J, Martinez-Frias J, Lopez-Martinez J (2007) Active tectonics, fault patterns, and stress field of

Deception Island: a response to oblique convergence between the Pacific and Antarctic plates. Jour South Am Earth Sci 23:256–268

Martí J (1991) Caldera-like structures related to Permo-Carboniferous volcanism of the Catalan Pyrenees (NE Spain). J Volcanol Geotherm Res 45:173–186

Martí J, Baraldo A (1990) Pre-caldera pyroclastic deposits of Deception Island (South Shetland Islands). Antarctic Sci 2:345–352

Martí J, Diez-Gil JL, Ortiz R (1991) Conduction model for the thermal influence of lithic clasts in mixtures of hot gases and ejecta. J Geophys Res 96(B13):21879–21885

Martí J, Vila J, Rey J (1996) Deception Island (Bransfield Strait, Antarctica): an example of volcanic caldera developed by extensional tectonics. In: McGuiere WC, Jones AP, Neuberg J (eds) Volcano instability on the Earth and other planets. Geol Soc London Spec Pub. 110, pp. 253–265

Martí J, Folch A, Macedonio G, Neri A (2000) Pressure evolution during caldera forming eruptions. Earth Planet Sci Lett 175:275–287

Martí, J., Geyer, A., Folch, A. (2009) A genetic classification of collapse calderas based on field studies, analogue and theoretical modelling. In: Thordarson T, Self S, Larsen G, Rowland SK and Hoslkuldsson A. (eds) Volcanology: the legacy of GPL Walker. Geol Soc London Spec Publ IAVCEI 2, pp. 249–266

Pallàs R, Smellie JL, Casas JM, Calvet J (2001) Using tephrochronology to date temperate ice: correlation between ice tephras on Livingston Island and eruptive units on Deception Island volcano (South Shetland Islands, Antarctica). Holocene 11(2):149–160

Paredes C, Pérez-López R, Giner-Robles J, De La Vega R, García-García A, Gumiel P (2006) Distribución espacial y zonificación tectónica de los morfolineamientos en la Isla Decepción (Shetland del Sur, Antártida). Geogaceta 39:75–78

Paredes C, De La Vega R, Pérez-López R, Giner-Robles JL, Martínez-Díaz JJ (2007) Descomposición fractal en subdominios morfotectónicos del mapa de lineamientos morfológicos. Bol Geol Min 118:775–787

Pedrera A, Ruiz-Consta A, Heredia N, Galindo-Zaldivar J, Bohoyo F, Marin-Lechado C, Ruano P, Somoza L (2013) The fracture system and the melt emplacement beneath the Deception Island active volcano, South Shetland Islands, Antarctica. Antarctic Sci 24:173–182

Pérez-López R, Giner-Robles JL, Martínez-Díaz JJ, Rodríguez-Pascua MA, Bejar M, Paredes C, and González-Casado JM (2007) Active tectonics on Deception Island (West-Antarctica): a new approach by using the fractal anisotropy of lineaments, fault slip measurements and the caldera collapse shape. In: AK Cooper and CR Raymond et al. (eds) Antarctica: a keystone in a changing world. Online Proceedings of the 10th ISAES, USGS Open-File Report 2007–1047, Short Research Paper 086, 4 p.; doi:10.3133/of2007-1047.srp086.

Putirka KD (2008) Thermometers and barometers for volcanic systems. Rev Mineral Geochem 69:61–120

Rey J, Somoza L, Hernandez-Molina FJ (1992) Formas de los sedimentos submarinos superficiales en el Puerto Foster, Isla Decepci6n, Islas Shetland delSur. In: Martínez-López J (ed) Geología de la Antártida Occidental Simposios T 3. III Congreso Geológico de España y VIII Congreso Latinoamericano de Geologia, Salamanca, pp 163–172

Rey J, Somoza L, Martinez-Frias J (1995) Tectonic, volcanic and hydrothermal event sequence on Deception Island (Antarctica). GeoMarine Lett 15:1–8

Rey J, Maestro A, Somoza L, Smellie JL (2002) Submarine morphology and seismic stratigraphy of Port Foster. In: Smellie JL, López-Martínez J (eds) Geology and geomorphology of Deception Island. British Antarctic Survey, Cambridge, pp 40–46

Risso C, Aparicio A (2002) Plutonic xenoliths in Deception Island (Antarctica). Terra Antartica 9:95–99

Smellie JL (1988) Recent observations on the volcanic history of Deception Island, South Shetland Islands. British Antarctic Survey Bulletin 81:83–85

Smellie JL (1989) Deception Island. In: Dalzieli WD (ed) Tectonics of the Scotia Arc, Antarctica. 28th International Geological Congress, Field Trip Guidebook T180. American Geophysical Union, Washington, DC, pp 146–153

Smellie JL (1999) The upper Cenozoic tephra record in the south polar region: a review. Glob Planet Chang 21:51–70

Smellie JL (2001) Lithostratigraphy and volcanic evolution of Deception Island, South Shetland Islands. Antarctic Sci 13:188–209

Smellie JL, Hofstetter A, Troll G (1992) Fluorine and boron geochemistry of an ensialic marginal basin volcano: Deception Island, Bransfield Strait, Antarctica. J Volcanol Geotherm Res 49:255–267

Smellie JL, López-Martínez J et al (2002) Text and geological and geomorphological maps. BAS GEOMAP series, Sheets 6-A and 6-B, Scale 1:25 000. In: Smellie JL L-MJ, Thomson JW, Thomson MRA (eds) Geology and geomorphology of Deception Island. British Antarctic Survey, Cambridge, 77p. + 3 folded maps

Valencio A, Mendía E, Vilas JF (1979) Palaeomagnetism and K-Ar age of Mesozoic and Cenozoic igneous rocks from Antarctica. Earth Planet Sci Lett 45:61–68

Vila J, Martí J, Ortiz R, Garcia A, Correig AM (1992) Volcanic tremors at Deception Island (South Shetland Islands, Antarctica). J Volcanol Geotherm Res 53:89–102

Vaun A, Robertson Maurice SD, Wiens DA, Panza GF (2005) Crustal and upper mantle S-wave velocity structure beneath the Bransfield Strait (West Antarctica) from regional surface. Tectonophysics 397:241–259

Walker GPL (1972) Crystal concentration in ignimbrites. Contrib Mineral Petrol 36:135–146

Walker GPL (1984) Downsag calderas, ring faults, caldera sizes and incremental caldera growth. J Geophys Res 89:8407–8416

Zandomeneghi D, Barclay A, Almendros J, Ibáñez JM, Wilcock WSD, Ben-Zvi T (2009) The crustal structure of Deception Island Volcano from P wave seismic tomography: tectonic and volcanic implications. J Geophys Res 11:B06310. doi:10.1029/ 2008JB006119